Investigating the three-body fragmentation dynamics of water via dissociative recombination and theoretical modeling calculations

Richard Thomas, Stefan Rosén, Fredrik Hellberg, Alik Derkatch, and Mats Larsson
Department of Physics, Stockholm University, SCFAB, S106 91 Stockholm, Sweden

Sheldon Datz
Physics Division, Oak Ridge National Laboratory, P.O. Box 2008, Oak Ridge, Tennessee 37831-6377

Richard Dixon
School of Chemistry, University of Bristol, Bristol, BS8 1TS, United Kingdom

Wim J. van der Zande
FOM Instituut AMOLF, Kruislaan 407, 1098 SJ Amsterdam, The Netherlands

(Received 2 October 2001; revised manuscript received 2 April 2002; published 23 September 2002)

We report an investigation into the three-body fragmentation of a triatomic molecule H_2O via the process of dissociative recombination (DR) of H_2O^+. At 0-eV center-of-mass reaction energy two competing three-body fragmentation channels are available, both leading to the production of ground state H atoms $H(^2S)$ but differing in the excitation state of the O atom fragment: $O(^3P)$ and $O(^1D)$. Using time- and position-sensitive detectors in a triple-coincidence experiment, the fragments from the DR reaction are monitored and their momentum vectors and angular distribution recorded. From these data we determine that during the recombination process, oxygen atoms are produced in the ratio of 3.5(0.5):1 for $O(^3P):O(^1D)$, and find that the molecular geometry is not conserved and that the available reaction energy is randomly distributed between both hydrogen atoms. Quasiclassical trajectory calculations having the same initial starting conditions as those in the experiment have been carried out using calculated and measured H_2O potential-energy surfaces, together with the knowledge of the various curve crossings, intersections, and estimations of the necessary coupling strengths. The results of these calculations, product state population distributions together with the geometries of the potential surfaces which contribute to the reaction, are compared to those observed in the experiment and allow questions to be answered on the dominance of three-body dissociation.

DOI: 10.1103/PhysRevA.66.032715 PACS number(s): 34.80.Ht, 33.15.Bh, 33.15.Dj, 82.20.Fd

I. INTRODUCTION

Water is one of the most important molecules for study in many branches of science. Its creation and destruction enables everything from rocket propulsion to simple organisms to function. It is considered one of the most important chemical signatures in determining biological life on (extra-solar) planets, and water was the second polyatomic molecule discovered in space [1]. Studying its destruction is of considerable importance to understanding the chemistry of many media.

Dissociative recombination (DR), a reaction process in which a molecular ion recombines with an often low energy electron and dissociates into neutral fragments, is extremely important in natural and man-made plasmas (see, e.g., [2]). DR reactions involving polyatomic ions and electrons play important roles in the chemical composition and evolution of such diverse media as astrophysical plasmas, i.e., interstellar molecular clouds, star-forming regions, inter- and intragalaxy medium, shock fronts, and planetary atmospheres. DR processes result not only in the loss of molecular species but also in the production of new radical species, which are often very reactive (see, e.g., [3–7]). To understand the role DR plays in the chemistry of these media, the rate coefficients and neutral product branching ratios arising from such processes are necessary. Ion storage rings have been extensively utilized for studying the different aspects of DR reactions [8,9]. Furthermore, recent advances in imaging techniques and technology have enabled the accurate measurement of the kinetic energy release of neutral fragments following DR of diatomic molecular ions in storage rings (see, e.g., [10–19]).

In spite of the apparent simplicity of DR processes, the development of a general theory able to predict product branching ratios for polyatomic ions has turned out to be difficult. There have been relatively few attempts at a theoretical approach to understanding such mechanisms. The model developed by Bates [20,21] argues that the most favored dissociative channel is that which involves the least rearrangement of valence bonds in the molecule. This theory then predicts that for ions of the type $X\,H_2^+$ (H_2X^+), the most favored dissociation channel is likely to involve the loss of a single hydrogen atom. However, almost all recent storage ring studies on DR of $X\,H_n^+$-type ions show a propensity for three-body breakup. For the ions H_3^+ [22], CH_2^+ [23], NH_2^+ [24], and H_2O^+ [25,26] the three-body channel constitutes 60–80% of the DR.

In all of the reactions where three-body fragmentation is so dominant over two-body fragmentation, it is not unreasonable to ask whether the three-body fragmentation is a two step process, i.e., the second step involves the fragmentation of a highly excited neutral product formed following the ini-

tial two-body fragmentation channel. A detailed investigation of this three-body dissociation channel might help to elucidate why these channels are more favored.

In an earlier paper [27] we reported the results from such a DR study for H_2O^+. The only other result reported in the literature from such DR experiments has been for H_3^+ [28], in which it is reported that H_3 dissociates almost exclusively with a linear geometry and not from the ionic and neutral ground state geometry which is equilateral. Of potential relevance to understanding the possible processes which are occurring in the breakup of H_3 and H_2O, there are results from photodissociation experiments in the literature, which report on the three-body fragmentation channels, e.g., photodissociation of state-selected H_3 [29,30] and photodissociation of H_2O at the Lyman-α wavelength [31–33]. Both Mordaunt *et al.* [31] and Dixon *et al.* [32] studied the photodissociation of water by monitoring the OH (+ H) yield, whilst Slanger and Black [33] looked at the yields of $H(^2S)$ and $O(^1D,^3P)$. It must be noted that direct comparisons are not possible, since dipole selection rules apply in the case of the photodissociation experiments, and these are significantly relaxed in the case of electron capture.

The present paper expands on the earlier published results [27]. The technique which was devised to enable the measurements to be made is explained in more detail, as are certain other new experimental steps which have been introduced to increase the accuracy and signal-to-noise of the data acquisition system. This paper also addresses in more detail the question of the dynamics of the DR process, i.e., the branching ratio, angular and reaction energy distributions, and, in particular, the question of the three-body fragmentation.

To answer these questions, two computational techniques have been employed. First, to try and model the three-body fragmentation to extract the branching ratios, angular and H atom energy distribution, a Monte Carlo simulation has been written, and the simulation, together with the results obtained, are explained in detail. This simulation does not model the dynamics of the dissociation itself, only the motion of the atoms after the molecule has fragmented and are sufficiently separated such that they do not feel each others influence.

To help understand the physics of the three-body dissociation, we looked at the experimental observations of Slanger and Black [33] and at the more recent experimental and trajectory model calculation observations reported by one of us (Dixon and co-workers [31,32]) on results from photodissociation of H_2O at Lyman-α wavelength (121.56 nm, 10.1998 eV). We have extended the scope of the trajectory model calculations such that the starting conditions of the initial wave packet on the potential surface match those of the current experiment. The results of these calculations, product state populations together with the knowledge of the geometry, energy and crossings of the potential surfaces involved in the dissociation, lead to a fuller understanding of the process and then allow conclusions to be drawn on the dominance of the three-body breakup.

Using the merged electron-molecular ion beams technique at two ion storage ring facilities, the dynamics of DR of H_2O^+ have been investigated. At a center-of-mass (c.m.) collision energy of $0^{+0.02}_{-0}$ eV, the branching ratio reported from the ASTRID [25] study is 0.22 for OH+H, 0.10 for O+H_2, and 0.68 for O+H+H, which is in good agreement with the results from the present CRYING study at a c.m. collision energy of $0^{+0.002}_{-0}$ eV, 0.20 for OH+H, 0.09 for O+H_2, and 0.71 for O+H+H [26]. The quoted errors in the collision energy arise from the limiting resolution of the electron energy.

For collisions occurring at zero c.m. energy, only two three-body product channels are energetically possible:

$$H_2O^+ + e^- \rightarrow O(^3P) + H(^2S) + H(^2S) + 3.04 \text{ eV} \quad (1)$$

$$\rightarrow O(^1D) + H(^2S) + H(^2S) + 1.07 \text{ eV}. \quad (2)$$

Almost all of the available energy released by the dissociation (KER) is divided between the two (light) hydrogen atoms. Furthermore, the difference in the energy available for the hydrogen atoms between the two channels means that any hydrogen atom with an energy $\gtrsim 1.1$ eV must come from decay to the ground electronic state, $O(^3P)$, of oxygen, i.e., channel (1).

Use of the storage ring technique to prepare H_2O^+ in its vibrational ground state, coupled with suitable detectors able to image the relative velocities of the three fragments, allows the geometry of the dissociating state and the excitation state of the O atom fragment to be investigated.

II. EXPERIMENT

The CRYRING facility has been described in detail elsewhere [12] and so here we just give a brief description and concentrate more on equipment developments which have been necessary to obtain the measurements reported here. Figure 1 shows the layout of the CRYRING apparatus. The H_2O^+ ions are created in a hollow cathode discharge source (JIMIS), then extracted and accelerated to 40 keV, mass analyzed, focused, and finally injected into the ring, which has a circumference of 51.6 m. The ions are then accelerated up to the required energy. For H_2O^+, the maximum beam energy is 5.33 MeV, although, as is discussed later, the ion beam was stored at slightly below this energy at 4.50 MeV (250 keV/amu). After acceleration, the ions coast in the ring before being dumped after 12 s, and the next injection started. During each revolution, the stored ion beam is merged over an effective interaction length of ≈ 0.85 m with a continuously renewed, magnetically confined monoenergetic electron beam having a current of ≈ 1.3 mA. This section of the ring is known as the ''electron cooler'' region. The electron beam is characterized by a transverse temperature of $kT_\perp = 2$ meV [34], which is achieved through its adiabatic expansion in the decreasing magnetic field on the way from the cathode to the interaction region. The longitudinal electron energy spread is reduced by the kinematic transformation to the moving frame, being typically in the order of $kT_\parallel = 0.1$ meV [35].

A 5-s interval between the injection of the ions and the start of data acquisition was sufficient to allow vibrational

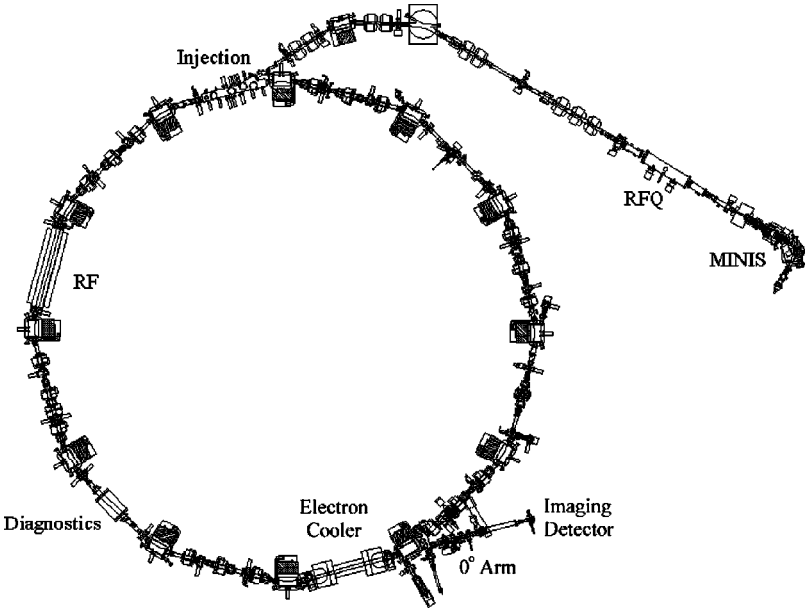

FIG. 1. Layout of the storage ring facility CRYRING. An H_2O^+ ion beam from the ion source JIMIS, which is situated on the MINIS platform, is injected in the ring at 40 keV and accelerated further to 4.6 MeV. In the ''electron cooler'' section the ions interact with electrons, the neutral products enter the ''0° arm'' and are detected on a 3D imaging detector 6.3 m from the center of the cooler.

relaxation of the ions into the ground state. Thermal coupling between the ions and cold electrons, through Coulomb interactions, during the passage of the ion beam through the velocity matched ($v_{ions}=v_{electrons}$) electron beam (4 cm in diameter) contributes to phase-space cooling of the ions and reduces the kinetic energy spread of the ions. As a consequence the diameter of the ion beam reduces to approximately 8 mm. The electron beam mainly serves as a high-density source of electrons for DR. The neutral products created in the cooler region were separated from the ion beam as they passed through the first dipole magnet following the cooler. These neutral products were then detected by the standard position- and time-sensitive detector array [18,19] mounted at a distance of ≈ 6.3 m from the midpoint of the electron cooler region.

The imaging detector used in this experiment consists of a stack of three microchannel plates (MCPs) and a phosphor screen (size $\Phi = 77$ mm, Hamamatsu) and is similar in design to that of Amitay and Zajfman [15], and in principle to that described in Peterson *et al.* [18] and Peverall *et al.* [19]. Fragment atoms from the DR of H_2O^+ strike the MCP stack and the created electron cloud generates flashes on the phosphor screen. Using a 70:30 beam splitter, these flashes on the phosphor screen are focused onto a multianode photomultiplier tube [(PMT), 16 lines, Hamamatsu], and onto a charge-coupled device (CCD) camera (64×64 pixels, Dalsa) via an image intensifier [(II), Proxitronic]. The CCD records the separation of the flashes, i.e., the fragments, on the phosphor, while the PMT is used to determine the difference in arrival time of the flashes (fragments) and also to act as a trigger to both the II and the CCD frame grabbing card which is situated in the data acquisition PC. Each of the 16 anodes of the PMT is connected to an input channel of a 16-channel constant fraction discriminator [(CFD), Le Croy 3420] and the 16-summed charge outputs from the CFD to a 16-input analog-to-digital converter [(ADC), Le Croy 4301B]. To remove signals arising from spurious events and thermal electrons in the MCP array, the detection system is operated in a gated mode, in which the II was switched on if three or more anodes of the PMT were triggered. Operating the detection system in this mode also gave rise to a strong reduction of signals arising from background processes, i.e., a contribution to the signal arising from collisional dissociation and electron-capture-induced dissociation of H_2O^+ with residual gas (G) molecules and those DR events leading to two-particle fragmentation, and allowed operation of the whole system at an event rate of about 600 Hz.

The contribution to the observed three-body events from dissociations arising from electron-capture reactions with the G molecules, typically H_2 and CH_4, in the reaction region—the ''electron cooler''—and in the sections of the ring immediately preceding and after the cooler needs to be ascertained, e.g.,

$$H_2O^+ + G \rightarrow O + H + H + G^+ + E(\mathrm{eV}). \tag{3}$$

To achieve this, separate experimental runs were carried out in which after the same 5-s cooling period of the ion beam, the electron beam was turned off, i.e., the electrons were not extracted from the cathode, and data were acquired in an identical fashion as for a ''normal'' run. The three-body background arising from these processes can then be determined and accounted for in the experimental data.

For homonuclear triatomic ions and all diatomic ions the detector described above would be sufficient to obtain all of the required experimental parameters. For studying H_2O^+, such a detection system is insufficient since it does not allow absolute identification of which neutral atom is which, i.e., which of the detected neutral atoms is oxygen or hydrogen. Since this information is essential to a complete understanding of the three-body DR process, a method of ''neutral-atom tagging'' was devised such that it was possible to differentiate between oxygen and hydrogen atom hits on the MCPs.

The ''neutral-atom tagging'' was achieved by mounting a thin aluminum foil of 5-mm diameter and 2.5 μm thickness in front of the first MCP in the detector array. The thickness

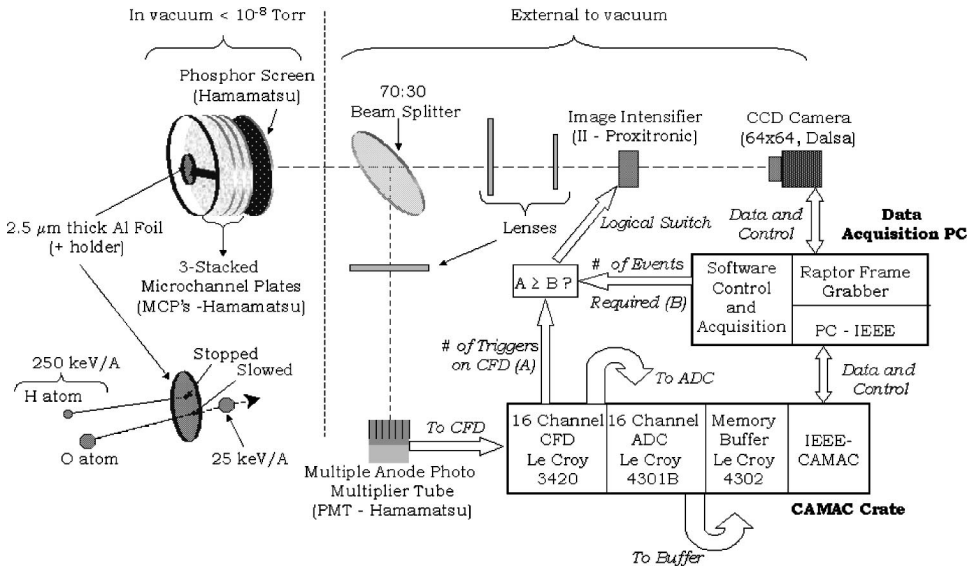

FIG. 2. Schematic of the detector and data acquisition system. Light emitted from the phosphor is split and focused onto a multiple anode photomultiplier tube [(PMT), Hamamatsu] and image intensifier [(II), Proxitronic]. The number of activated anodes of the PMT is determined by the Constant Fraction Discriminator [(CFD), Le Croy] which is situated in the CAMAC crate. With the best case scenario of one anode activated per light spot on the phosphor, i.e., one particle per anode, the II is used as a logical switch and if there have been sufficient anodes activated, i.e., in the DR experiment discussed here $B=3$, then the II is switched on to intensify the light emitted from the phosphor screen, with output phosphor of the II focused onto the CCD chip in the camera, with the information recorded by the camera read out by the RAPTOR (BitFlow Inc) frame-grabbing card. The analog-to-digital converter [(ADC), Le Croy] in the CAMAC crate is used, via the CFD, to determine the arrival time of the light flashes on the activated PMT anodes. The data acquisition computer controls and transfers data from the modules in the CAMAC crate via IEEE and internal frame-grabbing card via local bus.

of the foil was sufficient such that for an ion beam of 250 keV/amu, all hydrogen atoms, either arising from DR in the cooler or from collisional dissociation following interaction of the ions in the beam with rest-gas molecules, would not have sufficient energy to penetrate the foil. However, oxygen atoms from DR or collisional dissociation would always have sufficient energy to pass through the foil. Using this method, it was possible to ''tag'' atoms recorded in the position-sensitive detector, since a defined area of the detector could only be activated by oxygen atoms due to the foil. A schematic of the detection system is given in Fig. 2. The effectiveness of the foil at stopping H atoms with 250 keV of energy was checked using the TRIM code, running 500 trajectories for several ions. These data are listed in Table I. The TRIM code also allows us to calculate by how much the oxygen atoms are slowed by. This then can be used to calculate the time for the slowed oxygen atoms to strike the MCP plate, and their delay in comparison to the H atoms which are still moving with their full velocity. The calculated delay of the oxygen atoms is a distribution centered around 3.0 ± 0.1 ns.

TABLE I. Calculated energy loss for 250 keV/amu ions in 2.5 μm Al using TRIM code running 500 trajectories for each ion.

Ion	Initial energy (kev)	Final energy (kev)
H^+	250	stopped
D^+	500	242 ± 34
C^+	3000	267 ± 25
N^+	3500	321 ± 33
O^+	4000	410 ± 34

The separation of the two hydrogen atoms from the oxygen atom is related to the amount of energy they were given in the dissociation which is almost 3.04 or 1.07 eV for $O(^3P)$ and $O(^1D)$, respectively. They do not get all the available energy, since the oxygen atom also receives some. The three-dimensional (3D) distribution is mapped onto a two-dimensional (2D) imaging detector. The 2D separation of the hydrogen atoms from the oxygen on the imaging detector is therefore only a measurement of the *projection* of the released energy, and measurements made just using the CCD camera only give rise to 2D spectra. Use of the PMT as a timing system due to its fast triggering enables selection from this measured distribution, i.e., the first particle from a DR event can be used as a T_0 time trigger, and the subsequent triggering of the PMT by the arrival of the other particles from the DR event, their difference in arrival times relative to T_0 can be determined. Thus, a dissociation event perpendicular to the 2D detector will lead to events which have the *minimum* separation on the 2D detector but the *maximum* difference in arrival times relative to T_0. Dissociation parallel to the 2D detector will lead to events which have the *maximum* separation on the 2D detector but the *minimum* difference in arrival times relative to T_0. Using the timing information, it is possible to select events which dissociate parallel to the detector since the important parameters which need to be measured are from the information contained in the CCD image, and these data are termed three-

dimensional (3D) since they introduce time as an extra axial coordinate.

Using this foil-detector combination, images of individual DR events are taken. Event selection was based on the following criteria: that each CCD image contained three spots, that the positions of these spots in the frame coincided with those PMT strips triggered, and that one of the spots corresponds to oxygen, i.e., appears in the frame where the foil would be. Events fulfilling these criteria are then fully characterized, and in each event the distances of the O and two H atoms from the c.m. were determined.

Accepted events were analyzed for the following experimental parameters:

$$\left(d_{\mathrm{H}_1}^2 + d_{\mathrm{H}_2}^2 + \frac{m_{\mathrm{O}}}{m_{\mathrm{H}}} d_{\mathrm{O}}^2 \right)^{1/2}, \tag{4}$$

where $d_{\mathrm{H}_n}^2$ and d_{O}^2 are the transverse distances of the hydrogen atoms and oxygen atom from the c.m., respectively and m_{H} and m_{O} are the masses of the hydrogen and oxygen atom fragments, respectively. We then have

$$\chi_D = \angle(\text{H-c.m.-H}), \tag{5}$$

where χ_D is the angle between the H atom fragments measured in the plane of the detector with respect to the c.m. and

$$P(\text{c.m.-H}_i), \tag{6}$$

which is the frequency distribution of H atom transverse distances $(i=1,2)$ from the c.m. to determine the distribution of the available kinetic energy between the H atom fragments, and

$$T(\text{O-H}_i) \tag{7}$$

is the difference in arrival times between the oxygen and hydrogen atom fragments $(i=1,2)$.

The displacements of the fragments from the c.m. in the laboratory frame reflect directly the projected momenta of the fragments in the molecular frame. The total kinetic energy released in the reaction, given in Eqs. (1) and (2), is well defined. However, for each event the "energy in the plane of the detector," which varies according to the extent of out of plane motion, is proportional to the square of the mass-weighted three-body displacement of Eq. (4). We therefore represent the imaging data by this quantity, and refer to it throughout this paper as "TD" (total displacement). Since TD is roughly linear in the total displacement of, in particular, the hydrogen atoms, the measurement error in TD is approximately independent of its magnitude.

The maximum time difference between particles from a single DR event arriving at the detector is under 10 ns. Thus, all the PMT-CFD-ADC lines, i.e., the timing measurement system, have to be accurately calibrated. Since the oxygen atom has been slowed down by the foil, this also has to be accounted for. Care also has to be taken with the acquisition of data from the CCD such that the position of the spots in the frame and their arrival time at the detector are correctly matched in the software.

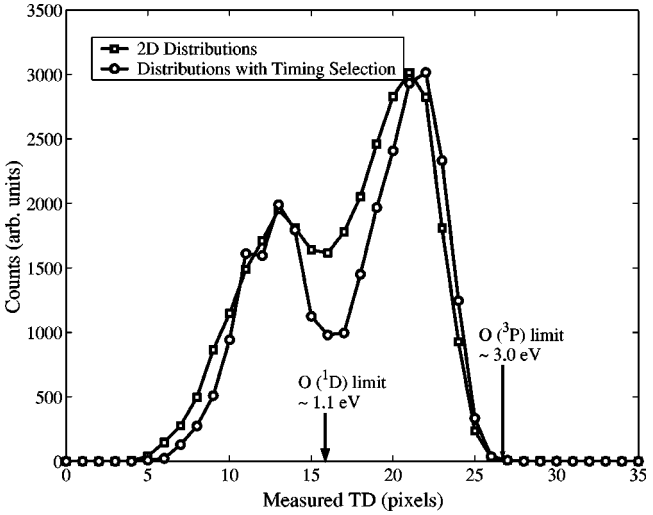

FIG. 3. The TD of all fragments (□) from the DR of H_2O^+, together with those (○) which arrive within $\Delta T \leqslant 800$ ps, the limiting resolution of the timing system.

Finally, throughout this paper, the calculated fragment separations are given in pixels as they are directly determined from the raw CCD frame data. The scaling factor between pixels and millimeters has been determined, and and one pixel is approximately 1.1 mm.

III. RESULTS AND DISCUSSION

The 2D TD distributions are plotted as open squares (□) in Fig. 3 for a c.m. collision energy of 0 eV. The two maxima in the distributions correspond approximately with the available dissociation energies to the channels producing $O(^3P)$ and $O(^1D)$, i.e., ≈ 1 and ≈ 3 eV, respectively and it can be concluded with certainty that both of the available channels are populated in the experiment. For the 2D distributions, two completely separated distributions are not possible. However, using the encoded timing information, it is possible to select those events which dissociate parallel to the detector. These data, for events which arrive within 800 ps of each other, are plotted as open circles (○) in Fig. 3. This technique has been shown to be extremely effective in the analysis of diatomic DR data, especially N_2^+ [18] and O_2^+ [19], in determining the branching ratio between populated fragmentation channels. Unfortunately, due to the relatively poor resolution in the timing measurement apparatus, coupled with the extra constraint of having three fragment atoms rather than two as in the case of the diatomic studies, it is seen that there is still some overlap between the two distributions and the extraction of an accurate branching ratio between these channels is still not directly possible from these data without some sort of fitting procedure. It is obvious, however, that the distributions obtained from the time-constrained analysis behave as expected, in that they sharpen up and become more distinct [18,19].

To get a meaningful measurement of the angular and H atom energy distributions we choose to analyze only those events which dissociated parallel to the detector and so minimize the aforementioned overlap. As can be seen from the

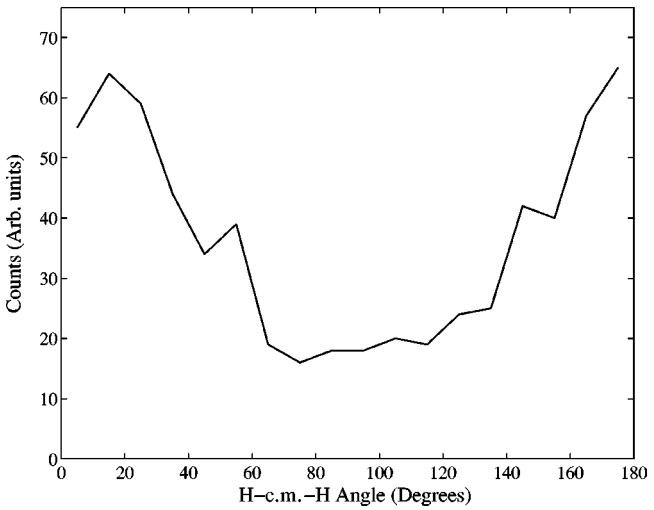

FIG. 4. Measured H-c.m.-H angles, binned in 10° steps, for fragments from events which have dissociated parallel to the detector, i.e., TD $\geqslant$23 pixels (a projected KER of $\geqslant$2.7 eV).

results illustrated in Fig. 3, it is not possible to do this for both $O(^1D)$ and $O(^3P)$ events since there is still overlap between the $O(^1D)$ and $O(^3P)$ channels. However, this is not the case for the maximum for the $O(^3P)$ channel, since these events are exclusively $O(^3P)$. Therefore, by selecting from the whole data set only those events which have TD $\geqslant$23 pixels, which corresponds to a projected kinetic energy release of $\geqslant$2.7 eV in the detector plane, we will be mainly sampling DR events which have dissociated parallel to the detector plane.

The results for the distribution of dissociation angles χ_D obtained from the analysis of these sampled data are plotted in Fig. 4. The intrabond angle of the ground-state ion and ground-state neutral is the same, and known to be $\sim$110° [36]. If we are to consider DR as an instantaneous reaction, such that subsequent to the electron capture the molecular bonds are broken on a time-scale shorter than a typical rotation, there would not be sufficient time for the energy of the reaction to be delocalized into the available molecular degrees of freedom. This initial approximation of the reaction suggests that angle of the molecule on dissociation could well be the same as or close to that of the ground-state ion. Analyzing only those data which match the criterion just detailed it can be seen, in the plot of the χ_D data displayed in Fig. 4, that this is observed not to be the case. In fact, it can be seen that there is a preference for dissociation occurring from a linear or small angle geometry. For either of these two cases to be true, it has to be necessary for the molecule to bend away from the minimum geometry of the ion and neutral ground state. Therefore, it is suggested that there must be a much larger gradient in the potential surface provided by the force in the bending motion of the molecule to take it away from the equilibrium position. The results obtained from the analysis of the energy distribution over the two H atoms are discussed later.

A. Monte Carlo simulation

To determine the branching ratio between the two three-body channels and to understand the measured angular distribution, a Monte Carlo simulation similar to that described in Ref. [30] was developed in MATLAB. Conservation of mass and momentum in the laboratory frame governs the breakup of a molecule with mass M and a velocity vector $\mathbf{V}_0$ into three fragments with masses m_i and velocity vectors $\mathbf{V}_i$,

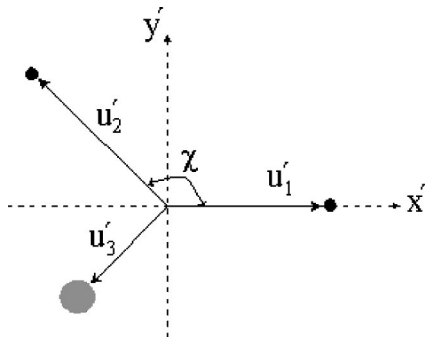

FIG. 5. Components of the fragment velocity vectors in the (x',y') plane of the molecule.

$$\sum_{i=1}^{3} m_i \mathbf{V}_i = M\mathbf{V}_0, \tag{8}$$

$$\sum_{i=1}^{3} m_i = M. \tag{9}$$

In the c.m. frame, conservation of momentum dictates the following requirements for fragments with momentum vectors $\mathbf{u}_i = m_i\mathbf{v}_i$ $(\mathbf{v}_i = \mathbf{V}_i - \mathbf{V}_0)$:

$$\sum_{i=1}^{3} \mathbf{u}_i = 0 \tag{10}$$

and these vectors define a plane in space which is represented by six independent components.

A coordinate system (x',y',z') can always be found for which all these vectors lie in one plane, and this is shown schematically in Fig. 5. To determine the components of these vectors, two independent parameters are introduced into the simulation. The first parameter χ represents the interfragment angle on dissociation. The second parameter ρ is defined such that

$$\rho = \frac{\mathbf{v}_2^2}{\mathbf{v}_1^2} \quad [0 \leqslant \rho \leqslant 1], \tag{11}$$

where $\mathbf{v}_{1,2}$ represents the velocity vectors of the two hydrogen atom fragments, with $\mathbf{v}_1$ the highest velocity. Since $m_1 = m_2$, $\mathbf{u}_1^2/\mathbf{u}_2^2 = \mathbf{v}_1^2/\mathbf{v}_2^2$ The fragment momentum vectors can be expressed by

$$\mathbf{u_1'} = (|\mathbf{u_1}|,0,0),$$

$$\mathbf{u_2'} = (|\mathbf{u_1}|\sqrt{\rho}\cos\chi, |\mathbf{u_1}|\sqrt{\rho}\sin\chi, 0), \tag{12}$$

$$\mathbf{u_3'} = (-|\mathbf{u_1}|(1+\sqrt{\rho}\cos\chi), -|\mathbf{u_1}|\sqrt{\rho}\sin\chi, 0),$$

where

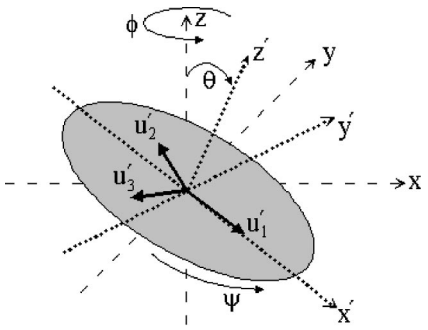

FIG. 6. Plot showing the transformation of the (x',y',z') coordinates of the c.m. frame into the (x,y,z) coordinates of the laboratory frame.

$$|\mathbf{u_1}| = \left[\frac{2m_1 E}{(1+\rho)+(m_1/m_3)(1+\rho+2\sqrt{\rho}\cos\chi)} \right]^{1/2}$$

and E is the total kinetic energy released (KER) in the reaction.

This coordinate system (x',y',z') is rotated with respect to the laboratory coordinate frame (x,y,z) by the Eulerian angles (θ,ϕ,ψ) as illustrated in Fig. 6, which has been adapted from [30]. Rotation within the (x',y') plane is defined by the angle ψ and the orientation of the z' axis in the laboratory frame is defined by the angles (θ,ϕ). For the selected coordinate system, the vectors $\mathbf{u}_i'$ are contained in the (x',y') plane and the vector $\mathbf{u}_1'$ is oriented along the x' axis. It is assumed that distributions of the Eulerian angles ϕ and ψ are random between 0 and 2π. The laboratory coordinate frame is oriented such that the neutral beam propagates along the x axis, and that the MCP detector lies in the y,z plane. This is an arbitrary choice and does not affect the results.

In the plane of the detector, the distance d_i traveled by a fragment with mass m_i from the beam axis is governed by the length of time t the extra momentum given by the dissociation, which occurs at a distance D from the detector, operates

$$d_i = \frac{\mathbf{u_i}'' t}{m_i}, \tag{13}$$

where $\mathbf{u_i}''$ is the momentum in the laboratory frame given to the fragment, and $t = D/\sqrt{2E_b/M}$ with E_b being the energy of the ion beam.

To enable comparison with the experimental data, exactly the same parameters are calculated in the simulation as were detailed earlier. As noted, it is important to give the correct weight to the rotation angles. The angles ϕ and ψ are random between 0 and 2π, with all angles being equally possible, while $\cos(\theta)$ is random between -1 and $+1$, with all points being equally likely.

B. Monte Carlo simulation results

It is possible to test the validity of this simulation. The intramolecular angle between the two fragments arising from the DR of a diatomic molecule can only be 180° and analytic functions to describe the KER distributions for such reactions are well known (see, e.g., [37]). The simulation for triatomic fragmentation can be made to simulate a diatomic fragmentation by fixing the intramolecular angle, $\chi = 180°$, and the ratio of the H atom energies, $\rho = 1$, i.e., both atoms get the same energy. With this symmetric arrangement of the three atoms, the O atom receives nothing of the available kinetic energy and the vectors describing the momentum of the H atoms are equal in length but point in directly opposite directions. Figure 7 plots the comparison between the projected TD results from the Monte Carlo simulation of a ''diatomic'' dissociation (○) with the analytical function describing such an isotropic distribution (solid line) for a ''true-diatomic'' dissociation [37]. Although not plotted, the simulated H-c.m.-H angle which would be measured in the detector frame is always 180°, indicating that the rotation procedure is working as expected.

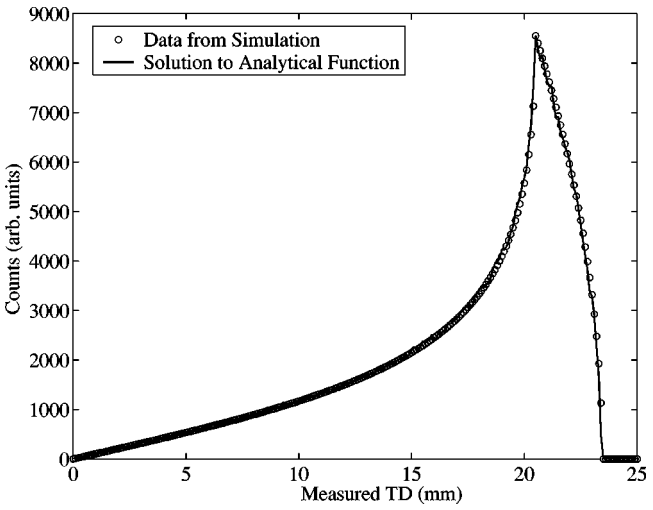

FIG. 7. Comparison of the TD results from the Monte Carlo simulation of a ''diatomic'' dissociation (○) with the analytical function describing such an isotropic distribution (-) for a ''true-diatomic'' dissocation [37].

1. Branching ratio

Since the simulation allows control over the energy available to each event, it is possible to calculate the branching ratio as follows: Two separate simulations were run with 10^6 events having, firstly, a KER of 1.07 eV and, secondly, a KER of 3.04 eV available for the reaction. The results of the projected distance distributions for both of these simulations were then independently scaled until the sum of the two distributions gave the best fit to the experimental data. The results from this process are displayed in Fig. 8. For the condition of best fit, the branching ratio is just the ratio of the two scaling factors, and is found to be 3.5(0.5):1 for $O(^3P):O(^1D)$, i.e., the production of ground-state oxygen atoms is favored by more than three to one. It must be noted that the simulation does not cover the full measured distribution, in that the simulated distribution is narrower than the measured distribution. This is mainly due to the resolution of the detection system, and such a parameter has not been included in the simulation, since justifying its magnitude would be difficult. The error quoted in the result is a repre-

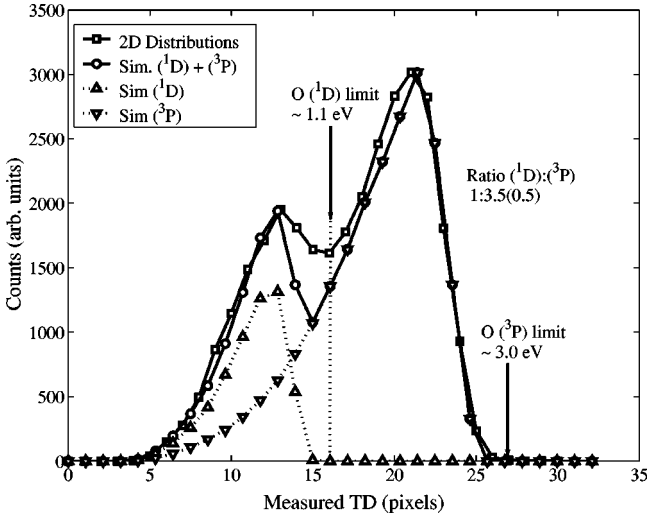

FIG. 8. Branching ratio determined by fitting two simulated distance distribution results for the production of $O(^1D)(\triangle)$ and $O(^3P)(\nabla)$, so that the sum of these distributions ($\bigcirc$) best reproduces the experimental data ($\square$).

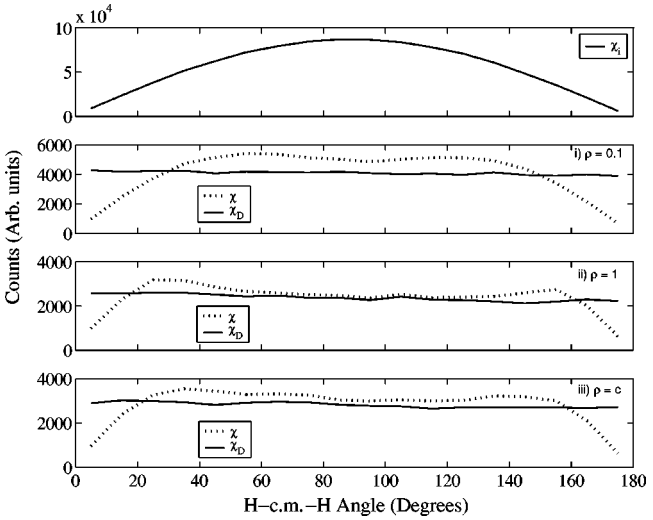

FIG. 9. The H-c.m.-H angle calculated for those simulated events producing $O(^3P)$ and having a projected KER of $\geqslant 2.7$ eV (TD $\geqslant 23$ pixels) in the plane perpendicular to the ion beam axis, i.e., the representation in the simulation of what would be measured by the detector in the experiment. The top panel shows the initial distribution of dissociation angles, χ_i, which is, for this test, unconstrained. Each of the three lower panels plot the angular distribution in the molecular (χ, dotted line) and detector (χ_D, solid line) planes for the three chosen values of ρ, i.e., $\rho=0.1$, $\rho=1.0$, and $\rho=c$ (a flat distribution between 0 and 1) from (i) to (iii), respectively.

sentation of the sensitivity in fitting the simulated distributions to those observed experimentally, and also includes a major experimental effect discussed here.

One of the major experimental effects which the simulation allows us to determine and be taken into consideration is the relative loss of ''events'' due to the presence of the foil. Since the channel producing $O(^1D)$ has a smaller kinetic energy release, preferentially more H atoms produced from this channel hit the foil than for those produced with $O(^3P)$. The simulation, of course, creates the foil in software and so it is trivial to determine this effect. The simulation indicates that 10% and 4% of all events which produce $O(^1D)$ and $O(^3P)$, respectively, are not measured in the experiment as one or both of the H atoms hit the foil and the event is then not analyzed. The relative loss of $O(^1D)$ events compared to that for $O(^3P)$ is then 6%, and this effect has been accounted for in the analysis procedure.

Furthermore, the TD profiles obtained from the simulated data showed no dependence on the values used in the simulation for the molecular angle or energy partition parameters χ and ρ, respectively, i.e., the branching ratio is relatively insensitive to these two parameters.

In our simulations we first seek to create the expected observations for the situation of the random orientation of the molecule in space, i.e., the absence of a preferred direction of dissociation as is the case for 0 eV collisions, the so-called isotropic distribution. In the next two sections, we investigate the effect of various distributions in χ and ρ. A completely randomized distribution in χ implies that the weighting of this function can be generated by $arccos[(r\times 2)-1]$, where t is a randomly generated number between 0 and 1, inclusive. It should be noted that this procedure yields a distribution of the projected angles on the detector that is uniform in the measured angle.

2. Angular distribution

The simulation also allows the angular distribution to be extracted from the data for those events which dissociated parallel to the detector plane. Since the H-c.m.-H angle χ on dissociation is a parameter in our simulation, the dependence of the measured angle on χ can be investigated. Two types of simulation to investigate the angular dependence were carried out. The first constrained the value of χ close to the known equilibrium bond angle of the ground neutral and ground ionic state of H_2O [36] ($\approx 110°$) such that $100° \leqslant \chi \leqslant 120°$. In the second instance χ was unconstrained, i.e., $0° \leqslant \chi \leqslant 180°$.

It is important to investigate the effect that the distribution of the available reaction energy might have on the angular distribution. The initial angle (χ) and the H atom energy distribution (ρ) are independent parameters in the simulation, and so the value of ρ should not effect those events which have a simulated KER of $\geqslant 2.7$ eV (TD $\geqslant 23$ pixels). To test this, results obtained from the simulation were considered for three settings of ρ, $\rho=0.1$, $\rho=1.0$, and $0\leqslant\rho\leqslant 1$, the latter case being a flat, random distribution denoted by $\rho=c$. These are displayed in the top, middle, and bottom panels, respectively, of Fig. 9. As can be seen, there is no strong dependence of the in-plane angle on the value of ρ used, since the calculated distributions have the same shape for each of the three cases.

Figures 10 and 9 illustrate results from the simulations where χ is constrained within $110°\pm 10°$ and unconstrained, i.e., $0 \leqslant \chi \leqslant 180°$, respectively. These distributions of χ, referred to as χ_i, are shown in the top panel of each figure. The bottom panel in each figure gives the calculated H-c.m.-H distribution in the molecular χ and detector χ_D planes for those events meeting the required criterion. It is

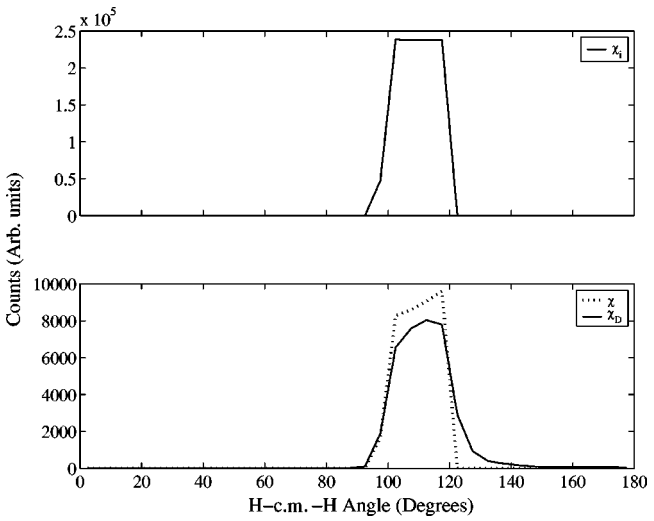

FIG. 10. For the simulation where the H-c.m.-H dissociation angle is constrained in the range $110° \pm 10°$ giving the distribution χ_i as shown in the top panel, the bottom panel shows the H-c.m.-H angular distribution in the molecular (χ, dotted line) and detector (χ_D, solid line) planes for those events dissociating to the O(^3P) limit with a projected KER of $\geqslant 2.7$ eV (TD $\geqslant 23$ pixels).

obvious that neither of the two cases discussed here matches the experimental data (Fig. 4). Conclusions can be drawn from the results of these two cases. For the case of the fixed initial angular distribution of χ_i, i.e., $110° \pm 10°$, the distribution measured in the detector plane (χ_D) is similar to that in the c.m. frame (χ), indicating that using this cut of projected TD events does not overly distort the angular distribution in the detection plane. Secondly, the random angular distribution of χ_i, i.e., $0 \leqslant \chi \leqslant 180°$, gives the result of a flat distribution in the detector plane, which is the expected result. It is noted that there is some effect to the angular distribution in taking this cut of projected TD events, and this has been investigated using the parameters available in the simulation.

It would be instructive to determine a possible initial H-c.m.-H angular distribution in the molecular frame which would, when used in the simulation, give rise to the H-c.m.-H angular distribution observed in the experiment. A good starting point is to look at the result given by dividing the χ_D distributions observed in the experiment (Fig. 4) with that obtained from the simulation where the H-c.m.-H angle is unconstrained (the bottom panel of Fig. 9). This ratio, illustrated in Fig. 11, indicates that the trial distribution should preferentially weight both smaller and more open angles over the random distribution. Such a trial distribution is plotted (solid line) in the top panel of Fig. 12, together with the random distribution (dotted line). The results in the molecular (χ, dotted line) and detector (χ_D, solid line) planes for those events meeting the required criterion are plotted in the middle panel of Fig. 12 and it can be seen that these data compare well with the observed experimental distribution, which is also plotted ($\square$, solid line) in the same panel.

Since the trial distribution leads to results which are a good comparison with the experimentally observed data, preferred molecular geometries at dissociation can be suggested by looking at the ratio of the trial χ_i distribution to that of random χ_i distribution, as illustrated in the bottom panel of Fig. 12. From this it can be seen that there is a preference for the molecule to dissociate from an open, near linear geom-

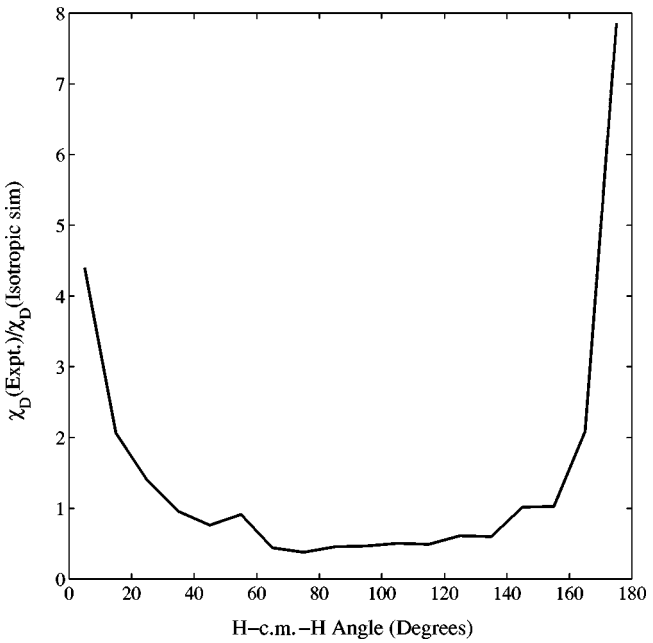

FIG. 11. The ratio of the χ_D distribution observed in the experiment (Fig. 4) to that obtained from the simulation where the H-c.m.-H angle is unconstrained, i.e., isotropic (Fig. 9, lower panel).

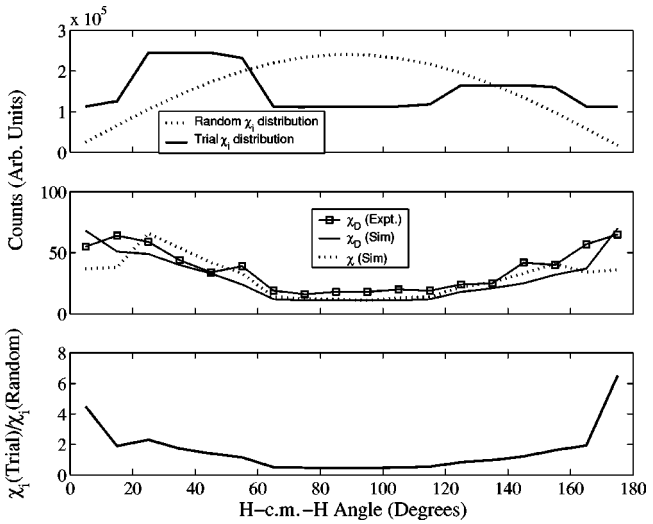

FIG. 12. For the trial χ_i distribution (solid line) plotted in the top panel, shown together with the random χ_i distribution (dotted line), the middle panel shows the H-c.m.-H angular distributions in the molecular (χ, dotted line) and detector (χ_D, solid line) planes for those events dissociating to the O(^3P) limit with a projected KER of $\geqslant 2.7$ eV (TD $\geqslant 23$k pixels). This compares well with the experimentally observed χ_D distribution (solid line, $\square$), also plotted in this panel. The bottom panel plots the ratio of the trial χ_i to random χ_i distributions.

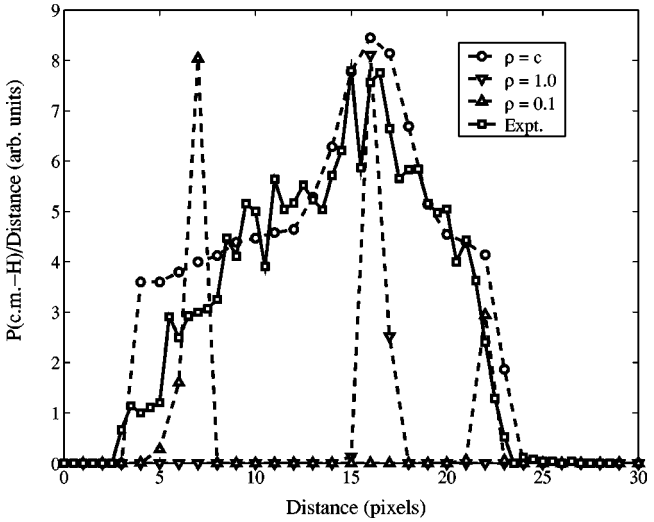

FIG. 13. Energy distribution for the two hydrogen atoms for events which occur parallel to the detector. Experimental data (□, solid line) compared to simulated data (dotted lines) for ρ = random (○), $\rho = 0.1$ (△) and $\rho = 1.0$ (∇).

etry as well as a small angle geometry, possibly near the H_2+O asymptotic channel. It is, therefore, concluded that the H_2O molecule changes its geometry significantly during the dissociation process.

3. H atom energy distribution

The other variable parameter in the simulation ρ represents how the available energy is split between the two hydrogen atoms. To compare with the measured experimental data, three models for the ρ parameter have been explored. In the first, the available energy is randomly distributed between the two hydrogen atoms; in the second, one gets most of the energy, and in the third, each atom gets half. These cases are represented by $0 \leqslant \rho \leqslant 1$ (a flat, random distribution denoted by $\rho = c$), $\rho = 0.1$, and $\rho = 1.0$, respectively. For those events in which dissociation occurs parallel to the detector, it is possible to directly extract the energy sharing information from these experimental data. Figure 13 compares the experimental results when the distribution in distance ($\approx$ momentum) is plotted with the corresponding simulation results for each of the three cases. The simulation resulting in the best matching of the experimental data is that for which the energy is a randomly distributed between the two hydrogen atoms, i.e., $0 \leqslant \rho \leqslant 1$.

4. Discussion on dynamics

It was shown above that H_2O^+ ions undergoing recombination with electrons at 0 eV display a strong preference to produce ground state $O(^3P)$ atoms over electronically excited $O(^1D)$ atoms. Furthermore, the 110° equilibrium angle of the ionic and neutral ground states is not observed in the DR reaction, indicative of a large bending motion during the dissociative process. In fact, a tendency towards linear geometries is found predominantly near 180° and, to a lesser extent, near 0°. Comparison with the simulation indicates that the sharing of available energy between the two hydrogen atoms during the reaction is best described with a flat, random distribution. It is worth noting that among the three chemically distinguishable channels, $O+H_2$ is only half as probable as OH+H which, taking into account the twofold degeneracy of the OH+H channel seems to indicate statistical branching into the two-body channels.

IV. THEORETICAL TREATMENT AND DISCUSSION

In 1999 Dixon and co-workers [32] investigated the photodissociation of H_2O using Lyman-α wavelength (121.56 nm, 10.1998 eV) photons employing the H atom Rydberg tagging technique; see Refs. [38] and [39] for a detailed description. They reported an even-odd intensity oscillation in the $OH(X\,^2\Pi\, v=0)$ product rotational distribution, and indicated that this observation was highly reproducible. For explanation, it was necessary to understand the role played by conical intersections in the potential energy surfaces of the exit channels.

In using a well-defined photon to excite a ground-state molecule, the initial excited state is also well defined. In the relevant case of using Lyman-α photons to excite ground-state H_2O, the excitation is to the second ($\tilde{B}$) excited state. Excitation to this state correlates, adiabatically, with a ground-state H atom and an excited state of the OH molecular partner ($A\,^2\Sigma^+$). However, the dominant channel from the photodissociation involves the production of OH in its ground state ($X\,^2\Pi$) and an H atom. It was concluded by Dixon *et al.* that this occurs via a nonadiabatic crossing from the second excited ($\tilde{B}$) state to potential-energy ground ($\tilde{X}$) states of H_2O [32].

The highly excited state of the $OH(X\,^2\Pi)$ product after excitation to the $\tilde{B}$ state, has been attributed to the presence of a conical intersection at a linear (H-O-H) geometry [40] of the excited- and ground-state potential-energy surfaces of H_2O, since dynamical calculations have shown that the high torque acting close to such an intersection in that geometry results in a high average rotational angular momentum. This particular conical intersection, for the linear approach of H to OH, arises from the crossing of the repulsive PES from $H+OH(X\,^2\Pi)$ with the attractive PES from $H+OH(A\,^2\Sigma^+)$.

Due to symmetry considerations, there is another conical intersection on the $\tilde{B}$ state surface for the O-H-H geometry. The importance of this intersection has been highlighted and discussed in relation to the reaction $H_2+O(^1D,^3P)$ [41,42], and, in relation to the potential role this intersection might have on the photodissociation of water, it has been shown in an earlier wave-packet calculation [31] that a small part of the dissociative flux on the $\tilde{B}$ state surface does, indeed, go towards this conical intersection and might play a large role in the dynamics of the dissociation on this surface [43].

The greatest obstacle to modeling such processes is the availability of accurate potential surfaces contributing to the dissociation and, in particular, in the regions around the conical intersections. This is highlighted by a much earlier calculation [44], in which the general distribution of the OH population distribution was well reproduced, but showed no evidence of the oscillations which were later observed ex-

TABLE II. All the combinations of states which have energies no higher than the ionization limit of H_2O. For each combination, the energy quoted is for the lowest rotational and vibrational level of a bound state. The given symmetries for the possible H_2O states assume only one plane of symmetry. Furthermore, it is to be expected that many of these states will be completely repulsive.

Combining states	Energy (eV)	States of H_2O
$H_2O^+ + e^-(d)$	12.616	$2\,^1A' + 3\,^1A'' + 2\,^3A' + 3\,^3A''$
$H_2O^+ + e^-(p)$	12.616	$^1A' + 2\,^1A'' + {}^3A' + 2\,^3A''$
$H_2O^+ + e^-(s)$	12.616	$^1A'' + {}^3A''$
$H + O(^1D) + H$	11.461	$3\,^1A' + 2\,^1A'' + 3\,^3A' + 2\,^3A''$
$H + O(^3P) + H$	9.494	$^1A' + 2\,^1A'' + 2\,^3A' + 4\,^3A'' + {}^5A' + 2\,^5A''$
$O(^1S) + H_2(X\,^1\Sigma_g^+)$	9.206	$^1A'$
$H + OH(A\,^2\Sigma^+)$	9.124	$^1A' + {}^3A'$
$O(^1D) + H_2(X\,^2\Sigma_g^+)$	6.983	$3\,^1A' + 2\,^1A''$
$H + OH(X\,^2\Pi)$	5.102	$^1A' + {}^1A'' + {}^3A' + {}^3A''$
$O(^3P) + H_2(X\,^1\Sigma_g^+)$	5.016	$^3A' + 2\,^3A''$
$[H_2O(\tilde{X}\,^1A_1)]$	0	$^1A'$

perimentally [32]. This problem was resolved in the later calculations [32] by introducing more accurately determined potential surfaces into the calculation [32,45,46].

The results from modeling the dissociation via these competing pathways introduced an interference pattern in the product rotation state, as observed in the experiment. The striking aspect of the calculation, as relates to the observations from the DR of H_2O^+, was the geometry of the molecule at the location of the two conical intersections, one with the atoms colinear as H-OH and the other as H-HO. The existence of a high-lying Rydberg state of water with a linear geometry has been known for the last decade [47], though the existence of an energy minimum for water with an H-HO geometry has been reported only recently, the results of Yarkony [45] and Dixon *et al.* [32] being the first to suggest such a state. The existence of a super bent Rydberg state of water has also been suggested [48]. The existence of both types of minimum energy geometries indicates that the molecule changes its intramolecular angle quite radically from the ground-state configuration to linear and bent on a very short time scale. The question which then arises from the observations and conclusions from the work of Dixon *et al.* [32] is ''are those same states of H_2O accessible during the dissociative recombination process?''

The problem of modeling the DR process is then related to knowledge of potential surfaces above the energy of Lyman-α, since the DR experiment represents combining states of $H_2O^+ + e^-$ at an energy of 12.616 eV. The states used in the earlier calculation [32] only needed those states up to 10.1998 eV. There is a total of 50 neutral states of H_2O having energies less than the ionization limit of 12.616 eV, and the possible combinations of these states are listed in Table II. In the case of each molecular combination, the quoted energy is that for the lowest vibrational and rotational level of a bound state. It must also be noted that the symmetries given for the possible states of H_2O assume only a single plane of symmetry.

Table III lists all the states of H_2O up to the $\tilde{B}\,^1A_1$ state and their adiabatic dissociation products. It is assumed that nonadiabatic interactions lead to radiationless transitions between some of these states, particularly through the conical

TABLE III. All the states of H_2O up to the $\tilde{B}\,^1A_1$ state, with their vertical excitation energies and adiabatic dissociation products. The lowest possible point group for nonrotating molecules has been assumed and nonadiabatic interactions can lead to radiationless transitions between some of these states, particularly through the conical intersection of the surfaces for $\tilde{B}\,^1A_1$ and $\tilde{X}\,^1A_1$. For those three-body channels indicated by an asterisk, it must be noted that $O(^1D) + H_2(X\,^1\Sigma_g^+)$ crosses $O(^3P) + H_2(b\,^3\Sigma_u^+)$ at $R(\text{H-H}) = 1.6$ Å.

State of H_2O	Energy (eV)	Bound bimolecular products	Three-body products
$2\,^1A'(\tilde{B}\,^1A_1)$	9.96	$H + OH(A\,^2\Sigma^+)/O(^1D) + H_2(X\,^1\Sigma_g^+)$	$H + O(^1D) + H$
$2\,^3A'(^3A_1)$	?	$H + OH(A\,^2\Sigma^+)$	$H + O(^3P) + H$
$2\,^1A''(^1A_2)$	9.60	$O(^1D) + H_2(X\,^1\Sigma_g^+)$	$H + O(^3P) + H^*$
$2\,^3A''(^3A_2)$	9.44	$O(^3P) + H_2(X\,^1\Sigma_g^+)$	$H + O(^3P) + H$
$1\,^1A''(\tilde{A}\,^1B_1)$	7.63	$H + OH(X\,^2\Pi)/O(^1D) + H_2(X\,^1\Sigma_g^+)$	$H + O(^3P) + H^*$
$1\,^3A''(\tilde{a}\,^3B_1)$	?	$H + OH(X\,^2\Pi)/O(^3P) + H_2(X\,^1\Sigma_g^+)$	$H + O(^3P) + H$
$1\,^3A'(^3A_1)$	?	$H + OH(X\,^2\Pi)/O(^3P) + H_2(X\,^1\Sigma_g^+)$	$H + O(^3P) + H$
$1\,^1A'(\tilde{X}\,^1A_1)$	0	$H + OH(X\,^2\Pi)/O(^1D) + H_2(X\,^1\Sigma_g^+)$	$H + O(^3P) + H^*$

TABLE IV. Geometries for the minima of those states with known adiabatic potential functions.

States of H_2O	Positions of minima (Å)	<H-O-H (deg)	Notes
$2\,^1A'(\tilde{B}\,^1A_1)$	0.98, 1.67	180	conical intersection
	1.00, 1.82	0	secondary conical intersection
$2\,^1A''(^1A_2)$	≈2.99, ≈2.99	≈15	shallow, O+H_2 like
$2\,^3A''(^3A_2)$	≈2.99, ≈2.99	≈15	shallow, O+H_2 like
$1\,^1A''(\tilde{A}\,^1B_1)$	at short Rs	≈105	H+OH repulsive, weak anisotropy
$1\,^1A'(\tilde{X}\,^1A_1)$	0.96, 0.96	105	and no inner minimum

intersection of the surfaces for $\tilde{B}\,^1A_1$ and $\tilde{X}\,^1A_1$. For those three-body product channels indicated by an asterisk in Table III, it is noted that $O(^1D)+H_2(X\,^1\Sigma_g^+)$ crosses $O(^3P)+H_2(b\,^3\Sigma_u^+)$ at $R(\text{H-H})=1.6$ Å.

Two thousand classical trajectories have been run for each of the five surfaces indicated for which there are published and/or available potential functions [46,49], i.e., those surfaces listed in Table III with quoted energies, and Table IV lists the geometries at the minima of these surfaces. Furthermore, the possibility of transitions between the $\tilde{B}$ and $\tilde{X}$ states have also been included. In each of the calculations, the total energy was approximately equal to that of the H_2O ionization limit.

The following assumptions were made in processing the calculations.

(1) The initial capture of an electron is to some high-lying electronic state(s), possibly with moderate vibrational excitation, but such states will be adiabatically bound on a short time scale. Both singlet and triplet states may be populated in this fashion.

(2) Large changes in nuclear geometry are necessary to permit transfer to any of the lower dissociative states.

(3) The surfaces indicated are widely separated in the Franck-Condon region, but all have strongly repulsive inner regions which reach the ionization energy when one or more bonds are compressed by up to 0.3 or 0.4 Å, depending on the state.

(4) The initial conditions have been reached by choosing six random numbers from a Gaussian distribution centered on the ionic geometry—the starting values of the three coordinates and three momenta, such that the energy is within a ± 50 cm^{-1} energy band. In a few cases, the starting conditions also involve angular distortions of up to 20°. This theoretical method is described more fully in Harrich *et al.* [43]. This includes details of the Wigner initial distribution, and the treatment of Landau-Zener transition probabilities at or at least near seams of conical intersections of potential-energy surfaces.

Next we discuss the results from the trajectory calculations on the available states, which are tabulated in Table V. A very wide range of angles between the directions of the two out-going H atoms is noted in all of the three-body dissociations. Furthermore, the lower the state of the H_2O neutral, the greater the necessary change in geometry to access the state. This is particularly true for the ground-state surface. To be certain that each diatomic product is stable, a check was made to determine if the internal energy was adiabatically bound within its centrifugally augmented potential. Certainly, in the case of $OH(A\,^2\Sigma^+)$ there is extensive predissociation of its higher levels [50]. Where this process is relevant, two numbers have been quoted. The first number neglects this predissociation and the second, in parentheses, allows for predissociation in a nanosecond or less, according to a reasonable model based on the known v,N behavior.

A. State of H_2O: $2\,^1A'(\tilde{B}\,^1A_1)$

If the OH predissociation is neglected for the $\tilde{B}$ state, the fragmentation is mainly a two-body process and the production of $H+OH(A\,^2\Sigma^+)$ dominates with a branching ratio of 88% and for the observed three-body fragmentation channels, the production ratio of $O(^3P)$ to that of $O(^1D)$ is

TABLE V. Dissociation outcomes for 2000 trajectories per initial state. In the case of $OH(A\,^2\Sigma^+)$ there is extensive predissociation of its higher levels. The first number neglects this predissociation and the second (in parentheses) allows for predissociation of these levels.

Products	States of H_2O $2\,^1A'(\tilde{B}\,^1A_1)$	$2\,^1A''(^1A_2)$	$2\,^3A''(^3A_2)$	$1\,^1A''(\tilde{A}\,^1B_1)$	$1\,^1A'(\tilde{X}\,^1A_1)$
$H+O(^1D)+H$	40	0	0	0	0
$H+O(^3P)+H$	179 (1003)	1999	1991	68	86
$H+OH(A\,^2\Sigma^+)$	1759 (935)	0	0	0	0
$O(^1D)+H_2(X\,^1\Sigma_g^+)$	18	1	0	0	0
$H+OH(X\,^2\Pi)$	4	0	0	1932	1914
$O(^3P)+H_2(X\,^1\Sigma_g^+)$	0	0	9	0	0

179:40, i.e., 4.5:1. If the possibility of the upper-lying OH states being predissociated is included, then the dominant product channel is the three-body channel producing $O(^3P)$, which has a branching ratio of 50% and relative production ratio over $O(^1D)$ of 25:1. In both of these situations, the production of $H_2(X\,^1\Sigma_g^+)$ is negligible, having a branching ratio of less than 1%.

B. State of H_2O:2 $^1A''(^1A_2)$

Dissociation from this surface does not involve the production of excited $OH(A\,^2\Sigma^+)$, and the dominant exit process is almost exclusively three body. There is only one of the three-body channels populated and that leads to the production of ground-state oxygen atoms. It is noted that the only other channel with a nonzero flux is that to the production of $O(^1D)+H_2(X\,^1\Sigma_g^+)$ but this channel is populated with a branching ratio of much less than 0.1%. The bound bimolecular product expected from this singlet surface is $O(^1D)+H_2(X\,^1\Sigma_g^+)$, and the only three-body channel leads to the production of triplet character oxygen, and so there must be an available curve crossing for this change of character. Such a curve crossing was observed in the calculation on the available surfaces and, as noted earlier, this crossing is between the surface for $O(^1D)+H_2(X\,^1\Sigma_g^+)$ and that for $O(^3P)+H_2(X\,^3\Sigma_u^+)$ at an H-H separation of 1.6 Å. Thus, that the channel $O(^1D)+H_2(X\,^1\Sigma_g^+)$ is relatively unpopulated indicates that the majority of the flux crosses over to the $O(^3P)+H_2(b\,^3\Sigma_u^+)$ giving rise to oxygen having triplet rather than singlet character. The coupling between these two channels comes from electron correlation at long range. Unfortunately, the magnitude of the coupling matrix element was not included in the *ab initio* calculations of the surfaces [49], and so the transfer of flux may have been overestimated due to the uncertainty in the strength of this coupling.

C. State of H_2O:2 $^3A''(^3A_2)$

This is the only surface of triplet character available for inclusion in the calculation. Dissociation from this surface is almost exclusively three body and as expected the only populated channel leads to the production of triplet (ground state) oxygen atoms. A two-body exit channel is also possible from this surface, with the production of $O(^3P)+H_2(X\,^1\Sigma_g^+)$, but that this is populated at under the 1% level.

D. State of H_2O:1 $^1A''(\tilde{A}\,^1B_1)$

Dissociation from this surface is predominantly two body, leading to the production of ground state OH, i.e., $H+OH(X\,^2\Pi)$ with a branching ratio of 97%. The only other populated exit channel from this surface is three body and leads to the exclusive production of ground-state oxygen. As for $2\,^1A''(^1A_2)$, this surface also has singlet character and the only three-body channel leads to the production of triplet oxygen. However, this surface differs from that of $2\,^1A''(^1A_2)$ in that there are two bound bimolecular products possible on this surface, i.e., $H+OH(X\,^2\Pi)$ and $O(^1D)+H_2(X\,^1\Sigma_g^+)$. Ground-state $OH(X\,^2\Pi)$ is stable against predissociation, and so this channel is unaffected by the curve crossing. However, it must be that the flux leading to $O(^1D)+H_2(X\,^1\Sigma_g^+)$ again crosses over to the $O(^3P)+H_2(b\,^3\Sigma_u^+)$ curve and allows the production of triplet oxygen from this singlet surface.

E. State of H_2O:1 $^1A'(\tilde{X}^1A_1)$

Dissociation from the ground-state surface is predominantly two body, leading to the production of ground state OH, i.e., $H+OH(X\,^2\Pi)$ with a branching ratio of 96%. The only other populated exit channel from this surface is three body and leads to the exclusive production of ground-state oxygen. As for the $1\,^1A''(\tilde{A}^1B_1)$ surface, there are two bound bimolecular products possible on this surface, i.e., $H+OH(X\,^2\Pi)$ and $O(^1D)+H_2(X\,^1\Sigma_g^+)$, and the same curve crossing detailed earlier can also explain the production of triplet (ground-state) oxygen from this singlet surface.

F. Discussion

Comparison of the above trajectory calculations with those on the same surfaces, but for initial conditions corresponding to excitation at the Lyman-α wavelength [43], shows that increasing the total energy by 2.4 eV leads to dramatic changes in the H_2O dissociation products. For example. three-body fragmentation is found to be significantly enhanced. This trend is much the same as that which has been observed experimentally when H_2S is excited at 157.6 nm or at 121.6 nm, with a similar energy difference of 2.3 eV [51]. The excitation energy for H_2S at 157.6 nm is approximately twice the dissociation energy (D_0^0) for loss of an H atom, as is that for H_2O at 121.6 nm. In both cases passage from the $\tilde{B}$ to the $\tilde{X}$ surfaces via conical intersections plays the dominant role in the dissociation to yield the products $H+SH/OH(X\,^2\Pi)$. But for H_2S this product channel has become negligible at 121.6 nm, even though the excitation is to the same $\tilde{B}$ state, and is replaced by the two-body products $H+SH(A\,^2\Sigma^+)$ and the three-body products $2H+S(^3P)$. The cause of this change is purely energetic. The increase in energy leads to much faster radial acceleration on the $\tilde{B}$-state surface, such that by the time the H-S-H angle has become linear the bonds are stretched well beyond their values for the conical intersections, thereby inhibiting the surface crossing (see Figs. 10 and 11 of [51]).

The present calculations show the same propensity for $OH(A\,^2\Sigma^+)$ as a product if starting from the $\tilde{B}$ state. However, DR is more complex, as it involves possible transitions to a large number of states, see for example Table III. Thus, we consider that the most important message of the calculations is the relative ease of three-body fragmentation. The calculations do not allow an exact comparison to our experimentally obtained results for several reasons. Firstly, the number of energetically accessible states near 12.6 eV is much larger than the limited set used in the present calculations. Secondly, in DR the whole manifold of triplet potential-energy surfaces may play an important role, even

enhanced by the multiplicity of these states. Repulsion between the hydrogen atoms occurs if these are formed in the triplet $b\,^3\Sigma_u^+$-state. In the case of a state with overall triplet character, this product state may be accompanied by an oxygen atom in the ^1D state. It is therefore possible that the under representation of the $O(^1D)$ product in the calculated three-body fragmentation channels may be attributed to the relative absence of the triplet states in the calculation compared to the known singlet surfaces. Thirdly, in the process of DR, a large number of quasibound Rydberg states may be accessible and such a Rydberg state may be formed which is subsequently predissociated by one of the many valence states.

There are many known structured Rydberg states, with lower Rydberg states tending to evolve into repulsive states, involving large changes in geometry [48]. It is possible that the initiation of DR is the reverse of vibrationally induced autoionization of low-l Rydberg states [48]. The electron is thereby captured into a vibrationally excited Rydberg state of low l, and n probably less than 10, but which also has a strong vibrational or nonadiabatic coupling to one or more of the repulsive valence states. Unfortunately, high capture efficiency would require that the transfer to the valence manifold is sufficiently rapid that the states involved would be hard to characterize experimentally through resolved rovibrational structures.

Coupling mediated through symmetric distortion of the two bonds would tend to favor the direct three-body dissociation route, but asymmetric distortion would initially favor bimolecular routes—but with possible sequential three-body decay. The more surfaces that are involved, the greater the tendency would be to a statistical product distribution, which would then favor $O(^3P)$ over $O(^1D)$, both by its higher degeneracy and by the higher available translational energy. In a purely statistical model, $O(^3P)$ would be favored over $O(^1D)$ by an electronic degeneracy factor of 9/5, multiplied by a factor of $\sqrt{3.04/1.07}$ arising from the translational degrees of freedom. This would mean that $O(^3P)$ is favored over $O(^1D)$ by a ratio of 3.0:1, which is in good, though maybe fortuitous, agreement with the experimentally observed ratio. The results of the trajectory calculations presented here, together with those of earlier studies (e.g., [43]), show that dynamical behavior can lead to a wide range of outcomes, according to the topology of the states involved. It is therefore likely that the true situation is at neither of these limits.

Our observations include angular correlation; all angles are observed with a preference for linear and closed geometry. The calculations described in Table IV also reveal a large spread over final dissociation angles. It is tempting to connect the preference for near linear and closed geometry to large amplitude bending motion during the dissociation, this motion being relatively slow near the turning points. What cannot be ignored is that for those states which are known, there is a large difference in the equilibrium configurations compared to that of the ionic state, which implies large torques in the molecule after interstate crossings.

V. CONCLUSIONS

The two available three-body channels leading to the production of either $O(^3P)$ or $O(^1D)$ from DR of H_2O^+ with 0-eV electrons have been investigated and the results analyzed. These data indicate that both of the available exit channels are accessed in the dissociation reaction. Analysis of those events which dissociate parallel to the detector suggests that there is no single sharply defined angle from which molecule dissociates, though there is a clear preference for open geometry and, to a lesser extent, a closed, small angle geometry.

To understand and investigate these observations, a Monte Carlo approach to model the break-up of the neutral molecule was undertaken. The simulation enabled several important experimental parameters to be investigated and calculated; the energy available, its partitioning between the neutral fragments, and the H-c.m.-H angle on dissociation.

The results of these simulations, the branching ratio to the production of $O(^3P)$ to $O(^1D)$, is determined from comparison of the experimental data with that produced from the simulation and is found to be 3.5(0.5):1, favoring the production of ground-state oxygen, $O(^3P)$. Analysis of the molecular angle for those events which dissociate parallel to the detector plane indicates an angular distribution which favors small-angle and linear geometries. Comparison of experimental data with the simulation also indicates that dissociation with the intermolecular angle ($110\pm10°$) of the H_2O ground-state ion and neutral is not preferred. Finally, analysis of the reaction energy distribution between the two hydrogen atoms shows the best comparison with experimental data for the case where the energy is randomly distributed between the H atoms, and not via a preferred mechanism, such as always equally.

Using the information observed experimentally and the insight gained from the simulations, trajectory calculations on neutral H_2O surfaces with known potential functions were performed to see if the these observations could be reproduced or understood using as good as possible numerical model. From the surfaces available for the calculation, the dominant products from the highest-energy surfaces, i.e., $2\,^1A'(\tilde{B}^1A_1)$, $2\,^1A''(^1A_2)$, and $2\,^3A''(^3A_2)$ favor three-body products over two body, though this is only true for dissociation from $2\,^1A'(\tilde{B}^1A_1)$ if $OH(A\,^2\Sigma^+)$ is predissociated. It may well be the case that three-body dissociation is the rule at these energies and not the exception.

The calculations show that the dynamical behavior leads to a wide range of product branching fractions, according to the topology of the surfaces involved. This also reinforces the requirement that these surfaces be known as accurately as possible and, if such surfaces were available, in three dimensions. On a purely statistical basis, $O(^3P)$ would be favored over $O(^1D)$ by a ratio of 3.0:1, calculated from the electronic degeneracy factor of 9/5 multiplied by $\sqrt{3.04/1.07}$ which arises from the translational degrees of freedom. While the purely statistical model results in a good agreement with the experimental observations, this may well be fortuitous.

Further experiments on the three-body break-up dynamics of different XH_2 are planned, such as NH_2^+ and CH_2^+ and

especially SH_2^+. SH_2 which, as has already been discussed, gives significant three-body fragmentation when excited at Lyman-α wavelengths and those potential-energy curves close to the ionization limit and which will be involved in the DR process are very well characterized.

ACKNOWLEDGMENTS

We would like to thank the CRYRING staff at the Manne Siegbahn Laboratory for their superb support and assistance. We also thank D. Zajfman (Weizmann Institute) and C. R. Vane (ORNL) for many valuable discussions and suggestions. This work was supported by the Swedish Research Council, the Swedish Foundation for International Cooperation in research and Higher Education, the IHP Program of the EC under Contract No. HPRN-CT-2000-00142. The work of W.vd.Z. is part of the research program of the Stichting voor Fundamenteel Onderzoek der Materie (FOM) and made possible by financial support by the Stichting voor Wetenschappelijk Onderzoek. The work of S.D. is sponsored by the U.S. Department of Energy, Offices of Basic Energy Sciences, Division of Chemical Sciences under Contract No. DE-AC05-00OR22725 with UT-Battelle, LLC. R.N.D. was supported by the University of Bristol.

[1] A. C. Cheung, D. M. Rank, C. H. Townes, D. D. Thornton, and W. J. Welch, Nature (London) **221**, 626 (1969).
[2] *Dissociative Recombination: Theory, Experiment and Applications*, edited by J. B. A. Mitchell and S. L. Guberman (World Scientific, Singapore, 1989).
[3] D. Smith and P. Spanel, Mass Spectrom. Rev. **14**, 255 (1995).
[4] R. M. Haberli, M. R. Combi, T. I. Gombosis, D. L. de Zeeuw, and K. G. Powell, Icarus **130**, 373 (1997).
[5] E. Herbst and H. H. Lee, Astrophys. J. **485**, 689 (1997).
[6] E. Herbst, Annu. Rev. Phys. Chem. **92**, 1473 (1995).
[7] *Dissociative Recombination: Theory, Experiment and Applications IV*, edited by M. Larsson, J. B. A. Mitchell, and I. F. Schneider (World Scientific, Singapore, 2000).
[8] M. Larsson, Rep. Prog. Phys. **58**, 1267 (1995).
[9] M. Larsson, Annu. Rev. Phys. Chem. **48**, 151 (1997).
[10] D. Zajfman, Z. Amitay, C. Broude, P. Forck, B. Seidel, D. Habs, D. Schwalm, and A. Wolf, Phys. Rev. Lett. **75**, 814 (1995).
[11] J. Semaniak, S. Rosén, G. Sundström, C. Strömholm, S. Datz, H. Danared, M. af Ugglas, M. Larsson, W. J. van der Zande, Z. Amitay, U. Hechtfischer, M. Grieser, R. Repnow, M. Schmidt, D. Schwalm, R. Wester, A. Wolf, and D. Zajfman, Phys. Rev. A **54**, R4617 (1996).
[12] C. Strömholm, J. Semaniak, S. Rosén, H. Danared, S. Datz, W. van der Zande, and M. Larsson, Phys. Rev. A **54**, 3086 (1996).
[13] D. Kella, P. J. Johnson, H. B. Pederson, L. Vejby-Christensen, and L. H. Andersson, Phys. Rev. Lett. **77**, 2432 (1996).
[14] W. J. van der Zande, J. Semaniak, V. Zengin, G. Sundström, S. Rosén, C. Strömholm, S. Datz, H. Danared, and M. Larsson, Phys. Rev. A **54**, 5010 (1996).
[15] Z. Amitay and D. Zajfman, Rev. Sci. Instrum. **68**, 1387 (1997).
[16] L. H. Andersson, P. J. Johnson, D. Kella, H. B. Pederson, and L. Vejby-Christensen, Phys. Rev. A **55**, 2799 (1997).
[17] D. Kella, L. Vejby-Christensen, P. J. Johnson, H. B. Pederson, and L. H. Andersson, Science **276**, 1530 (1997).
[18] J. R. Peterson, A. Le Padellec, H. Danared, G. H. Dunn, M. Larsson, Å. Larson, R. Peverall, C. Strömholm, S. Rosén, M. af Ugglas, and W. J. van der Zande, J. Chem. Phys. **108**, 1978 (1998).
[19] R. Peverall, S. Rosén, J. R. Peterson, M. Larsson, A. Al-Khalili, L. Vikor, J. Semaniak, R. Bobbenkamp, A. le Padellec, A. N. Maurellis, and W. J. van der Zande, J. Chem. Phys. **114**, 6679 (2001).
[20] D. Bates, Astrophys. J., Lett. Ed. **306**, L45 (1986).
[21] D. Bates, J. Phys. B **24**, 3267 (1991).
[22] S. Datz, G. Sundström, Ch. Biederman, L. Broström, H. Danared, S. Mannervik, J. R. Mowat, and M. Larsson, Phys. Rev. Lett. **74**, 896 (1995).
[23] Å. Larson, A. Le Padellec, J. Semaniak, C. Strömholm, M. Larsson, S. Rosén, R. Peverall, H. Danared, N. Djurić, G. H. Dunn, and S. Datz, Astrophys. J. **505**, 459 (1998).
[24] L. Vikor, A. Al-Khalili, H. Danared, N. Djurić, G. H. Dunn, M. Larsson, A. Le Padellec, S. Rosén, and M. af Ugglas, Astron. Astrophys. **344**, 531 (1999).
[25] L. Vejby-Christensen, L. H. Andersen, O. Heber, D. Kella, H. B. Pedersen, H. T. Schmidt, and D. Zajfman, Astrophys. J. **483**, 531 (1997).
[26] S. Rosén, A. Derkatch, J. Semaniak, A. Neau, A. Al-Khalili, A. Le Pedellec, L. Vikor, R. Thomas, H. Danared, M. af Ugglas, and M. Larsson, Faraday Discuss. **115**, 295 (2000).
[27] S. Datz, R. Thomas, S. Rosén, M. Larsson, A. M. Derkatch, F. Hellberg, and W. van der Zande, Phys. Rev. Lett. **85**, 5555 (2000).
[28] D. Strasser, L. Lammich, S. Krohn, M. Lange, H. Kreckel, J. Levin, D. Schwalm, Z. Vager, R. Wester, A. Wolf, and D. Zajfman, Phys. Rev. Lett. **86**, 779 (2001).
[29] U. Müller, Th. Eckert, M. Braun, and H. Helm, Phys. Rev. Lett. **83**, 2718 (1999).
[30] U. Müller and P. C. Cosby, Phys. Rev. A **59**, 3632 (1999).
[31] D. H. Mordaunt, M. N. R. Ashfold, and R. N. Dixon, J. Chem. Phys. **100**, 7360 (1994).
[32] R. N. Dixon, D. W. Hwang, X. F. Yang, S. Harich, J. J. Lin, and X. Yang, Science **285**, 1249 (1999).
[33] T. G. Slanger and G. Black, J. Chem. Phys. **77**, 2432 (1982).
[34] H. Danared, A. Kälberg, L. Liljeby, and K.-G. Rensfelt, in *Proceedings of the 6th European Particle Accelerator Conference, Stockholm*, edited by S. Myers, L. Liljeby, Ch. Petit-Jean-Genaz, J. Poole, and K.-G Rensfelt (IOP, London, 1998), p. 1031.
[35] H. Danared, G. Andler, L. Bagge, C. J. Herrlander, J. Hillke, J. Jeansson, A. Kälberg, A. Nilsson, A. L. Paál, K.-G. Rensfelt, U. Rosengård, J. Starker, and M. Ugglas, Phys. Rev. Lett. **72**, 3775 (1994).
[36] D. Zajfman, A. Belkacem, T. Graber, E. P. Kanter, R. E. Mitchell, R. Naaman, Z. Vager, and B. J. Zabransky, J. Chem. Phys. **94**, 2543 (1991).

[37] L. Vejby-Christensen, D. Kella, H. B. Pederson, and L. H. Andersen, Phys. Rev. A **57**, 3627 (1998).
[38] L. Schnieder, W. Meier, K. H. Welge, M. N. R. Ashfold, and C. M. Western, J. Chem. Phys. **92**, 7027 (1990).
[39] L. Schnieder, K. Seekamp-Rahn, E. Wrede, and K. H. Welge, J. Chem. Phys. **107**, 6175 (1997).
[40] K. Weide and R. Schinke, J. Chem. Phys. **87**, 4627 (1987).
[41] T.-S. Ho, T. Hollebeek, H. Rabitz, L. B. Harding, and G. C. Schatz, J. Chem. Phys. **105**, 10472 (1996).
[42] G. C. Schatz, J. Chem. Phys. **83**, 5677 (1985).
[43] S. A. Harich, D. W. H. Hwang, X. F. Yang, J. J. Lin, X. Yang, and R. N. Dixon, J. Chem. Phys. **113**, 10073 (2000).
[44] R. N. Dixon, J. Chem. Phys. **102**, 301 (1995).
[45] D. R. Yarkony, Mol. Phys. **93**, 971 (1998).
[46] R. van Harrevelt and M. C. van Hemert, J. Chem. Phys. **112**, 5777 (2000).
[47] S. T. Pratt, J. L. Dehmer, and P. M. Dehmer, Chem. Phys. Lett. **196**, 469 (1992).
[48] G. Theodorakopoulos, I. D. Petsalakis, and M. S. Child, J. Phys. B **29**, 4543 (1996).
[49] R. van Harrevelt and M. C. van Hemert (private communication).
[50] D. R. Yarkony, J. Chem. Phys. **97**, 1838 (1992).
[51] P. A. Cook, S. R. Langford, R. N. Dixon, and M. N. R. Ashfold, J. Chem. Phys. **114**, 1672 (2001).